minerals

MDPI

Article

Garnets from Val d'Ala Rodingites, Piedmont, Italy: An Investigation of Their Gemological, Spectroscopic and Crystal Chemical Properties

Valeria Diella [1,*], Rosangela Bocchio [2], Nicoletta Marinoni [2], Franca Caucia [3], Maria Iole Spalla [2], Ilaria Adamo [4], Antonio Langone [5] and Lucia Mancini [6]

1 Institute of Environmental Geology and Geoengineering (IGAG), Section of Milan, National Research Council, 20133 Milan, Italy
2 Department of Earth Sciences "Ardito Desio", University of Milan, 20133 Milan, Italy; rosangela.bocchio@unimi.it (R.B.); nicoletta.marinoni@unimi.it (N.M.); iole.spalla@unimi.it (M.I.S.)
3 Department of Earth Sciences, University of Pavia, 27100 Pavia, Italy; caucia@crystal.unipv.it
4 Italian Gemological Institute (IGI), 20123 Milan, Italy; ilaria.adamo@igi.it
5 Institute of Geosciences and Earth Resources (IGG), Section of Pavia, National Research Council, 27100 Pavia, Italy; langone@igg.cnr.it
6 Elettra-Sincrotrone Trieste S.C.p.A., 34149 Basovizza (Trieste), Italy; lucia.mancini@elettra.eu
* Correspondence: valeria.diella@cnr.it; Tel.: +39-02-5031-5621

Received: 6 November 2019; Accepted: 23 November 2019; Published: 26 November 2019

Abstract: In Val d'Ala (Piedmont, Western Alps, Italy), the more interesting rocks for the mineralogical research are represented by rodingites (rich in mineralized veins and fractures) associated with serpentinites in the eclogitized oceanic crust of Piemonte Zone, south of Gran Paradiso Massif. Among the vein-filling minerals, garnets are the most appreciated as mineral specimens and, in less degree despite their vivid and rich colors, for their potential as gem-quality materials. This study provides a complete gemological characterization of five faceted samples and offers new information by means of Synchrotron X-ray computed micro-tomography imaging gem features. Electron-probe microanalysis (EMPA) and laser ablation–inductively coupled plasma–mass spectrometry (LA–ICP–MS) established that the chemical composition of garnets from different localities, resulted both close to pure andradite, enriched in light rare earth elements (LREE) with a positive Eu anomaly, and grossular-andradite solid solution (grandite), enriched in heavy rare earth elements (HREE). X-ray powder diffraction analyses indicate the possible coexistence of almost pure grossular and andradite. A spectroscopic approach, commonly used with gem-like material, by Raman and diffuse reflectance infrared Fourier transform (DRIFT) spectroscopy, completes the characterization of the samples. The new data on the textural and geochemical features of the grandite and andradite garnets suggest local growth processes under various chemical and oxidation conditions of metasomatic and metamorphic fluids interacting with the host-rocks. Garnets represent long-lasting mineral records of the complex geological history of the Val d'Ala rodingitic dikes during their oceanic- and subduction-related metamorphic evolution.

Keywords: garnet; rodingites; Val d'Ala; Piedmont; Western Alps; Italy

1. Introduction

Val d'Ala (Piedmont, Italy) is internationally renowned for mining activity of minerals used for practical and decorative purposes. The more interesting minerals, garnet, "mussite" (a fibrous variety name of diopside), vesuvianite, and epidote have been well known since the 18th century. The orange–brown grossular-garnets, known with the variety name "hessonite", were used in the past as precious gemstones in the traditional costumes of the valley and as a sign of engagement. The grossular

crystals, up to 2 cm in size, are generally found in rodingites and show a color from dark brown to red orange with large variation in the habit and complex micro crystal faces. Most of the deposits produced euhedral crystals, that have been sampled for mineral collections, scientific investigations, and jewelry (Figure 1). A second type of garnet, variety name "topazolite", belonging to the andradite end member, is also present in this valley but the small size of the crystals prevents their use in jewelry. The crystals show only rhombic-dodecahedral habit and cover the walls of thin and irregular fractures occurring in the mussite with associated magnetite. Rare andradite crystals occur as "melanite" and "demantoid" varieties.

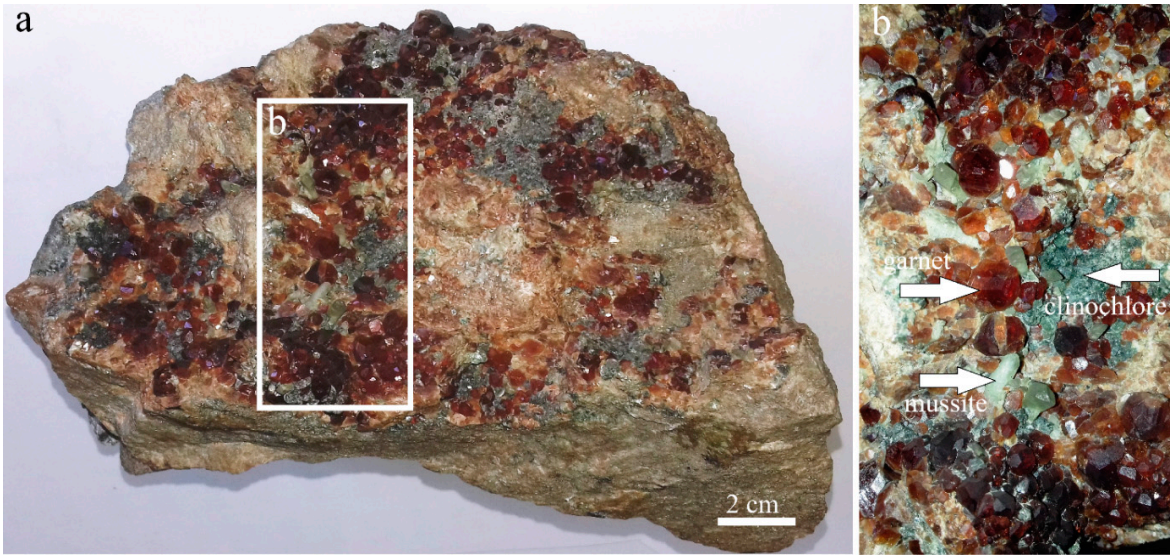

Figure 1. (**a**) Orange hessonite crystals filling fractures in rodingite from Val d'Ala (Museum of the Earth Sciences Department, University of Milan); (**b**) close-up showing the mineral assemblage filling the fracture. Photos by R. Bocchio.

In the first decades of last century, detailed studies have been performed mainly focusing on the morphological and chemical properties of the garnet, and on the more notable occurrences of rodingite layers and lenses along the valley, representing the main sources of high-quality crystals [1–3]. Recently, Maletto and Piccoli [4] published a monograph of great interest for museum and private collections dedicated to all Val d'Ala minerals.

The significant scientific and economic value of garnet from Val d'Ala is documented in literature, even if in recent times the mineralogical, petrological, and structural investigations on this mineral are lacking. In this light, we have undertaken this study, aimed to provide a complete mineralogical and gemological characterization that may enhance their potential use as gem material and their role in metamorphism. The chemical and physical properties elucidated in this study may further the understanding of the metamorphic kinematics experienced by the Val d'Ala ultramafic and rodingite host rocks, and their evolution in the subduction of Mesozoic ocean lithosphere during the Alpine orogeny. In particular, the different geodynamic environments in which rodingites can form must be considered. In fact, rodingites are Si-undersaturated and Ca-rich rocks that can form as a result of the metasomatic interaction between serpentinites and mafic dykes at the ocean floor or after fluid-assisted recrystallization during subduction and collision [5–14]. Garnet is indeed a litmus paper as it is always present in the diagnostic assemblages in each of these different petrogenetic environments.

The studied samples belong to the Bazzi historical collection preserved in the Museum of the Department of Earth Sciences of the University of Milan, Italy. The faceted samples were characterized by standard gemological methods, Synchrotron X-ray computed micro-tomography (SR-μCT) and Raman spectroscopy. Mineral fragments coming from the same localities and garnet country-rocks were analyzed by X-ray powder diffraction (XRPD), diffuse reflectance infrared Fourier

transform spectroscopy (DRIFTS), and electron microprobe (EMPA–WDS) combined with laser ablation-inductively coupled plasma-mass (LA–ICP–MS) techniques.

2. Geological Setting

Val d' Ala (Figure 2) is an east valley underlain by metaophiolites of the Piemonte Zone of the Western Alps between the Gran Paradiso (to the North) and Dora–Maira Penninic continental nappes. These Mesozoic oceanic rock sequences mainly consist of ultramafites, metagabbros, metabasalts, and calcschists, which underwent Alpine metamorphism under greenschist- and blueschists-facies conditions. These multiple facies reflect the polyphase evolution recorded from Mesozoic ocean lithosphere deformation in the Tertiary Alpine subduction and collisional tectonics ([15–17] and references therein). During Alpine subduction, Val d'Ala metaophiolites re-equilibrated at $P \geq 1.3$ GPa and T = 425–550 °C, as estimated from eclogite relics variably preserved during exhumation-related greenschist-facies [17]. Mineral assemblages of metabasites and ultramafites ([15–17] and references therein) indicate that these ophiolites recorded an ocean floor-related metamorphic imprint, under conditions (zeolite-, prehnite-pumpellyite- and greenschist-facies) similar to those suggested for other metaophiolites from Western Alps [10]. Their qualitative PT (Pressure-Temperature) evolution as deduced from the literature is synthesized in Figure 2d where the low- and high-pressure stability fields of different garnet-bearing assemblages inferred from polymetamorphic rodingites of Betic Cordillera, in Southern Spain [18] are reported (light-pink fields). The ultramafic rocks consist of antigorite serpentinite bodies that represent the most widespread rock-type of Val d'Ala, and contain from decametric to metric lenses and layers of rodingites. These rocks are intersected by abundant veins that have attracted the interest of many researchers since the beginning of 1800 ([6,19] and references therein). Rodingites occur in many localities all along Val d'Ala, from the high part of the valley, West of the village of Balme, to the lower part of the valley, East of the village of Ala di Stura near Mount Curbassera. In all occurrences, the rodingites are very heterogeneous with structural and mineralogical features that record a complex tectonic origin. The rodingite-forming minerals are mainly Ca-rich garnet, epidote, diopside, chlorite, and vesuvianite, with minor titanite and opaque minerals [16]. A complete list of all the minerals as well as the detailed description of the main occurrences of rodingites are already reported by [3]. The mineralogical richest and most known locations for finest grossular are Testa Ciarva and Roch Neir (I and II; labelled No.1, 2, and 3 in Figure 2c) where the serpentinite cliffs contain rodingite layers up to 2 m that are commonly boudinaged. South of Roch Neir, in Mount Tovo serpentinites (labelled 4 in Figure 2c), mineralized veins host garnets with a rounded and globular shape. Finally at Curbassera (labelled 5 in Figure 2c), grossular concentrations occur both in lenses of brown rodingite and in blocks of debris in a landslide fallen in the 18th century. Our samples came from the above-mentioned famous localities.

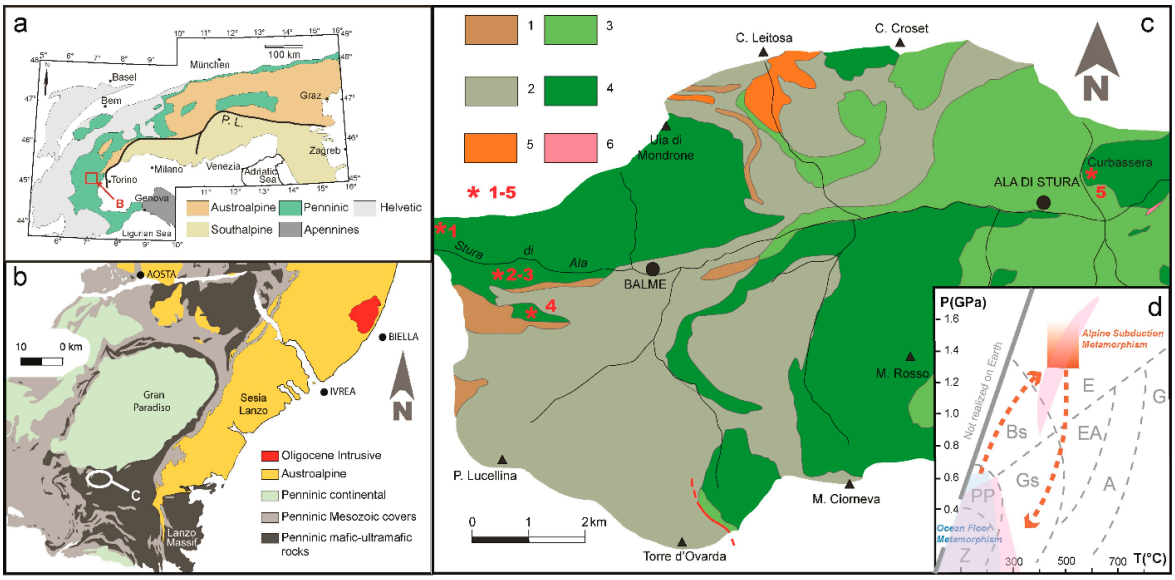

Figure 2. Geologic outline of Val d'Ala garnet-bearing rocks: (**a**) tectonic sketch map of the European Alps; (**b**) tectonic scheme of the Western Alps with Val d'Ala location; (**c**) simplified geological map of Val d'Ala modified after [16,20]. Legend: Metaophiolites of the Piemonte Zone: 1 = calcschist; 2 = metabasalt; 3 = metagabbro; 4 = serpentinite; 5 = metagranitoid with K-feldspar porphyroclasts (Gran Paradiso nappe–Penninic continental crust); 6 = fine-grained gneiss (Sesia-Lanzo Zone–Austroalpine continental crust); sampling localities: red asterisks: 1 = Testa Ciarva; 2, 3 = Roch Neir I, II; 4 = Mount Tovo; 5 = Curbassera. (**d**) Qualitative P-T evolution of Val d'Ala metaophiolites as inferred from [10,17]. See discussion in the text. Orange square = estimated metamorphic conditions of eclogite facies in Val d'Ala [17]. Metamorphic facies are after [21]: A = amphibolite, Bs = blueschist, E = eclogite, EA = epidote-amphibolite, G = granulite, Gs = greenschist, PP = prehnite-pumpellyite, Z = zeolite. Light-pink fields = low- and high-pressure conditions for garnet growth in polymetamorphic rodingites from Betic Cordillera–Southern Spain [18].

3. Materials and Methods

Twelve samples from different localities were selected for this study and are described in Table 1. The samples range from light yellow to dark red in color. The reddish garnets, from 1 cm to 3 cm in size with various crystalline faces (cube, trapezoedron, rhombic-dodecahedron, and hexoctahedron), may be deformed whereas the light yellow samples are smaller, up to 4 mm in size, clear and only rhombic-dodecahedron in shape.

Table 1. Description of the studied garnets.

Sample	Locality	Color	Analytical Techniques			
1	Roch Neir I	dark red	electron microprobe (WDS)		powder XRD	
2	Roch Neir I	light yellow	electron microprobe (WDS)	LA–ICP–Mass spectrometry	powder XRD	DRIFT spectroscopy
3	Testa Ciarva	from light yellow to jacinth and dark red	electron microprobe (WDS)	LA–ICP–Mass spectrometry	powder XRD	DRIFT spectroscopy
4	Roch Neir II	dark red	electron microprobe (WDS)	LA–ICP–Mass spectrometry		DRIFT spectroscopy
5	Roch Neir II	dark red	electron microprobe (WDS)			
6	Curbassera	from light yellow to jacinth and dark red	electron microprobe (WDS)	LA–ICP–Mass spectrometry		
7	Mount Tovo	from light yellow–green to dark red	electron microprobe (WDS)	LA–ICP–Mass spectrometry	powder XRD	DRIFT spectroscopy
8 faceted stone	Roch Neir II	orange red	specific gravity	refractive index	Micro-Raman spectroscopy	
9 faceted stone	Roch Neir II	orange red	specific gravity	refractive index	Micro-Raman spectroscopy	Microfocus X-ray computed μ-tomography
10 faceted stone	Roch Neir II	orange red	specific gravity	refractive index	Micro-Raman spectroscopy	Microfocus X-ray computed μ-tomography
11 faceted stone	Testa Ciarva	reddish orange	specific gravity	refractive index	Micro-Raman spectroscopy	Microfocus X-ray computed μ-tomography
12 faceted stone	Testa Ciarva	reddish orange	specific gravity	refractive index	Micro-Raman spectroscopy	

Five faceted samples (three from Roch Neir II, samples 8–10, and two from Testa Ciarva, samples 11, 12) were examined by standard gemological methods at the laboratories of the University of Pavia, Italy, in order to determine their refractive index, hydrostatic specific gravity and microscopic features. The refractive indices were measured with a Krüss refractometer (1.45–1.80 range) using ordinary light source with a sodium filter (589 nm) and a methylene iodide as a contact liquid (n = 1.80). A Mettler hydrostatic balance was used to determine the specific gravity in bi-distilled water. The ultraviolet fluorescence was investigated with a short (254 nm) and long (366 nm) wavelength ultraviolet Wood lamp. The color was determined with a GIA Color Table; often the crystals are slight polychrome.

The Microfocus X-ray computed micro-tomography (CT) analyses of two cut samples (10 and 11) were performed at laboratory X-ray μCT scanning using the TomoLab station at the Elettra synchrotron facility in Basovizza (Trieste, Italy). The μCT system is equipped with a sealed microfocus X-ray source (L9181, Hamamatsu Photonic, Iwata, Japan) and delivers a polychromatic beam in a Voltage range of 40 kV to 130 kV with a maximum current of 300 μA and a minimum focal spot size of 5 μm. The used detector consisted of a full frame CCD imager (4008 × 2672 pixels) coupled to a Gadox scintillator screen by a fiber-optic taper. The water-cooled CCD camera has a 12-bit dynamic range and an effective pixel size of 12.5 μm^2 × 12.5 μm^2. The experimental parameters used for the X-ray μCT scans are reported in Table 2. The slice reconstruction was carried out using the commercial software COBRA (Exxim Computing, Pleasanton, CA, USA) based on the Feldkamp algorithm [22], which also allows us to correct beam hardening artefacts [23]. 3D visualization through volume rendering of the analyzed samples were obtained by the commercial software VGStudio 2.2 (Volume Graphics).

Table 2. Experimental parameters used for the laboratory X-ray microtomography measurements (d_1 and d_2 represent the source-to-sample and the source-to-detector distances, respectively).

Sample	d_1 (mm)	d_2 (mm)	Voltage (kV)	Current (μA)	Voxel Size (μm)	Al Filter Thickness (mm)	Exposure Time (sec)
10	80	400	130	61	5.0	1.5	6.1
11	80	500	90	89	4.0	0.75	8.25

Seven samples from different localities were polished and analyzed by electron microprobe (EMPA) and inductively coupled plasma–mass spectroscopy (LA–ICP–MS): five massive garnets samples varying from 1–2 mm (2 and 7) to 3–4 cm in size (1, 4 and 5) embedded in epoxy resin, and two thin sections (3 and 6) of rock containing garnets in their matrix.

Backscattered electron (BSE) images and quantitative chemical analyses of major and minor elements were obtained with the JEOL JXA-8200 electron microprobe in wavelength dispersion mode (EMPA–DS) at the laboratory of the Department of Earth Sciences of the University of Milan, Italy, under the following conditions: 15 kV accelerating voltage, 5 nA beam current, and a count time of 60 s on peak and 30 s on the background, with a 1 μm diameter beam. Natural minerals were used as standards and the rough data corrected for matrix effects using a conventional ΦρZ routine in the JEOL software package (Japan Electron Optics Laboratory).

Rare earth and selected trace elements were determined by laser ablation–inductively coupled plasma–mass spectroscopy (LA–ICP–MS) at IGG-CNR Laboratory of Pavia, Italy. Wherever possible measurement spots were chosen at the same or close to the EMPA points. The instrument consisted of a 193 nm Excimer laser (Geolas) coupled to an Agilent 8900 triple quadrupole ICPMS. The spot size was 55 μm, using NIST SRM 610 glass as an external standard and ^{29}Si as an internal standard, as analyzed by microprobe. Precision and accuracy estimated on the USGS basaltic glass standard BCR2 and NIST612 were better than 10%.

Four fragments (~500 μm) from samples 1–3, and 7 were selected for powder X-ray diffraction measurements. The analyses were performed at the Department of Earth Sciences of the University of Milan, by a Panalytical X'Pert-PROMPD X'Celerator X-ray powder diffractometer, using CuKα radiation (λ = 1.518 Å), at a beam voltage of 40 kV and a current of 40 mA. X-ray powder diffraction

patterns were collected over the 9–120° range of the scattering angle 2θ, with steps of 0.01° 2θ and a count time of 50 s per step. The lattice parameters of the garnet samples were determined by using Si (NBS SRM 640b) as an internal standard and the General Structure Analysis System (GSAS) software was used to process XRPD data [24,25].

Besides standard gemological testing, four faceted samples were analyzed by Raman spectroscopy at the laboratories of the University of Pavia. Micro-Raman scattering measurements were conducted using a Horiba Jobin-Yvon Xplora Plus single monochromator spectrometer (with a grating of 2400 groove/mm) equipped with an Olympus BX41 microscope. Raman spectra were excited by the 532 nm line. The spectrometer was calibrated to the silicon Raman peak at 520.5 cm^{-1}. The spectral resolution was ~2 cm^{-1} and the instrumental accuracy in determining the peak positions was ~0.56 cm^{-1}. Raman spectra were collected in the spectral range 50–1250 cm^{-1} and 3000–3800 cm^{-1} for 5 s averaging over 40 accumulations.

Diffuse reflectance infrared Fourier transform spectroscopy (DRIFTS) was performed on four samples at the Italian Gemological Institute (IGI), using a Perkin Elmer Frontier FTIR, equipped with the Praying Mantis diffuse reflection accessory. The spectra of the samples (2–4, and 7) were collected between 8000 cm^{-1} to 450 cm^{-1}, using $LiTaO_3$ as detector. A resolution of 4 cm^{-1} was adopted and a total of 128 scans were recorded and averaged for each sample.

4. Results and Discussion

4.1. Gemological Properties and 3D Visualisation

The vivid, intense and rich colors, ranging from reddish orange to orange red, make the faceted samples of gemological interest (Figure 3). The luster is vitreous; the diaphaneity is transparent/translucent. The gems have been cut from samples with a combination of the rhombic dodecahedron {100} and trapezohedron {211} crystal form. The inhomogeneous color of some samples may be due to the presence of crystalline inclusions such as clinochlore, diopside, calcite veinlets, or fractures. Their physical and optical properties are reported in Table 3. The measured gravity ranges from 3.63 g/cm^3 to 3.66 g/cm^3, in agreement with the literature data for solid solution grossular/andradite [26]. All the analyzed gems are inert to long and short UV.

Figure 3. Faceted garnets described in Table 3.

Table 3. Physical and optical data.

Gem	Weight (ct)	Gravity (g/cm^3)	Refraction Index	Color (GIA)	Cut/Shape
8	3.04	3.66	>1.81	orange red	Brilliant oval
9	5.6	3.63	>1.81	orange red	Fantasy triangular
10	4.22	3.66	>1.81	orange red	Emerald rectangular
11	0.45	3.65	>1.81	reddish orange	Brilliant round
12	0.33	3.66	>1.81	reddish orange	Brilliant round

More details were provided by the 3D visualisation of faceted samples 10 and 11 and their renderings are shown in Figure 4. In Figure 4a, the tomographic results highlight the occurrence of small and irregular crystals (labeled *garnet 11-2*) widespread on the surface of the gem (*garnet 11-1*). The lighter gray-scale values associated to *garnet 11-2* might reflect its slightly different chemical composition with respect to *garnet 11-1* and attributed to the presence of a Fe-richer phase. This hypothesis is consistent with the XRPD refinement results of sample 3 from the same locality, indicating the coexistence both of grossular and of andradite (see below; Section 4.2).

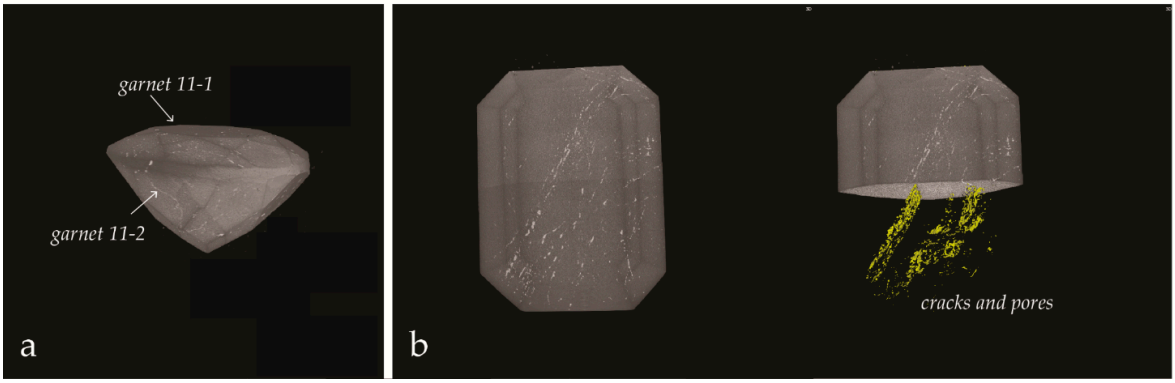

Figure 4. Garnet 3D visualization: (**a**) volume renderings of sample 11; (**b**) volume renderings and segmented pores and cracks of sample 10.

Furthermore, the 3D rendering with the corresponding iso-surfaces of the fractures and pores of sample 10 are shown in Figure 4b. A widespread microcracking is highlighted inside the garnet and is characterized by cracks mostly iso-oriented. Pores appear micrometric in size with an irregular shape and randomly distributed inside the whole volume. The reconstructed slices show that the cracks are mostly empty and, only in few cases, are filled with mineral phases, which have grayscale values very similar to *garnet 11-2* and could be attributed to the crystallization of andradite.

4.2. Chemical Composition and Crystallographic Properties

We analyzed five massive samples and two thin sections where the mineral paragenesis consists mainly of garnet, diopside, clinochlore, amphibole, and rutile/titanite. Fabric of the host-rodingites varies from massive to foliated, generally banded (summarized description of thin sections are synthesized in Table 4).

The relative quantities of grossular and andradite compared to all remaining components are plotted in Figure 5 and averaged chemical analyses for samples 2, 7, 1, 4, 5 and selected analyses for thin sections, samples 3 and 6, are reported in Table 5. The rare earth elements (REE) and trace elements concentrations are presented in Table 6.

Table 4. Textural and mineralogical characters of studied thin sections from samples 3 and 6. The short side of thin sections microphotographs is 6 mm and 10 mm for samples 3 and 6, respectively.

	Mineral Assemblages	Texture	
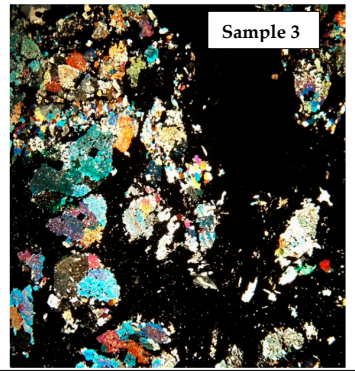	Garnet, clinopyroxene, Mg-rich chlorite, tremolite, calcite, magnetite, rutile.	Massive: garnet occurs in aggregates or in veins interstitial between diopside polygonal and seriate aggregates. Large grainsized diopside is cloudy and wrapped by clear fine-grained polygonal diopside grains. Garnets show complex Grs–Adr zoning (different gray patchy zones in the BSE image on the left) that are intersected by late Adr-rich veins.	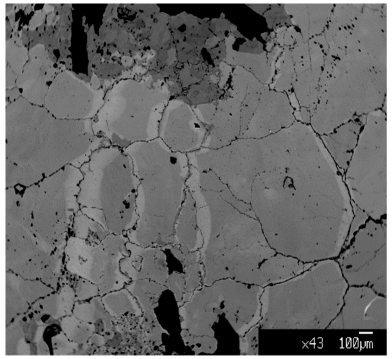
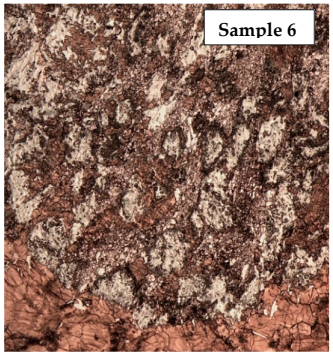	Garnet, clinopyroxene, Mg-rich chlorite, tremolite, magnetite, rutile, titanite, and calcite.	Foliated: garnetite vein at high angle with the Alpine foliation that is marked by chlorite-diopside lenticular aggregates and garnet trails and elongated aggregates. Compositional pattern of garnet is complex: in garnetite veins Adr-rich grains occur, whereas in fine-grained aggregates complex and oscillatory Grs–Adr zoning occurs, as shown in the BSE image on the left.	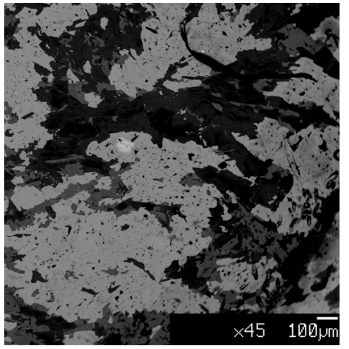

Table 5. Electron microprobe analyses of the Val d'Ala garnets (wt %).

Sample	2		7		1		4		5		3		6	
	Average 5 pts	**st. dev.**	**Average 50 pts**	**st. dev.**	**Average 8 pts**	**st. dev.**	**Average 13 pts**	**st. dev.**	**Average 43 pts**	**st. dev.**	**c1-6**	**c1-1**	**c3b-42**	**c3b-43**
SiO_2	35.98	0.24	35.53	0.24	38.25	0.24	37.84	0.37	37.75	0.43	38.67	39.67	37.32	38.35
TiO_2	0.02	0.02	0.35	0.14	1.14	0.13	1.58	0.38	1.54	0.41	0.54	0.18	1.53	0.74
Al_2O_3	0.60	0.23	0.15	0.05	15.07	0.52	14.03	0.82	14.20	0.97	17.75	20.06	15.00	19.99
Cr_2O_3	0.01	0.01	0.04	0.04	0.02	0.02	0.01	0.02	0.02	0.02	0.02		0.05	0.14
FeO_{tot}	27.39	0.40	27.75	0.27	9.52	0.36	10.53	0.79	10.30	0.81	7.43	3.59	11.79	11.40
MnO	0.10	0.03	0.06	0.04	0.26	0.05	0.27	0.04	0.28	0.05	0.22	0.11	0.78	0.51
MgO	0.11	0.02	0.16	0.04	0.12	0.04	0.17	0.04	0.18	0.06	0.43	0.27	0.17	1.25
CaO	33.21	0.10	33.33	0.11	35.17	0.25	34.94	0.34	34.76	0.31	34.71	36.20	32.48	27.54
Total	97.42		97.38		99.55		99.38		99.03		99.78	100.08	99.12	99.91
Number of ions on the basis of 24 oxygens														
Si	6.032		5.976		5.945		5.917		5.923		5.935	6.002	5.867	5.905
Ti	0.003		0.044		0.133		0.185		0.182		0.063	0.021	0.181	0.085
Al	0.118		0.031		2.761		2.586		2.626		3.211	3.577	2.779	3.627
Cr	0.001		0.005		0.002		0.001		0.002		0.003	-	0.007	0.017
Fe^{3+} *	3.812		3.899		1.087		1.212		1.176		0.791	0.381	1.122	0.379
Fe^{2+} *	0.029		0.004		0.150		0.166		0.180		0.163	0.073	0.428	1.089
Mn	0.015		0.008		0.035		0.035		0.038		0.029	0.014	0.103	0.067
Mg	0.027		0.039		0.027		0.040		0.041		0.098	0.061	0.040	0.286
Ca	5.964		6.006		5.856		5.854		5.844		5.708	5.868	5.471	4.544
Prp	0.45		0.64		0.44		0.66		0.68		1.64	1.01	0.66	4.77
Alm	0.48		0.07		2.48		2.72		2.95		2.71	1.21	7.08	18.20
Sps	0.24		0.13		0.57		0.58		0.62		0.49	0.23	1.71	1.12
Adr	95.78		97.73		26.71		29.83		28.84		18.81	9.35	25.68	7.16
Uv	0.03		0.13		0.05		0.03		0.06		0.06	0.00	0.15	0.32
Grs	2.96		0.18		66.49		61.62		62.41		74.80	87.68	60.58	66.81
Shorl	0.07		1.12		3.39		4.75		4.65		1.57	0.53	4.57	2.12

* calculated on the basis of stoichiometry [27].

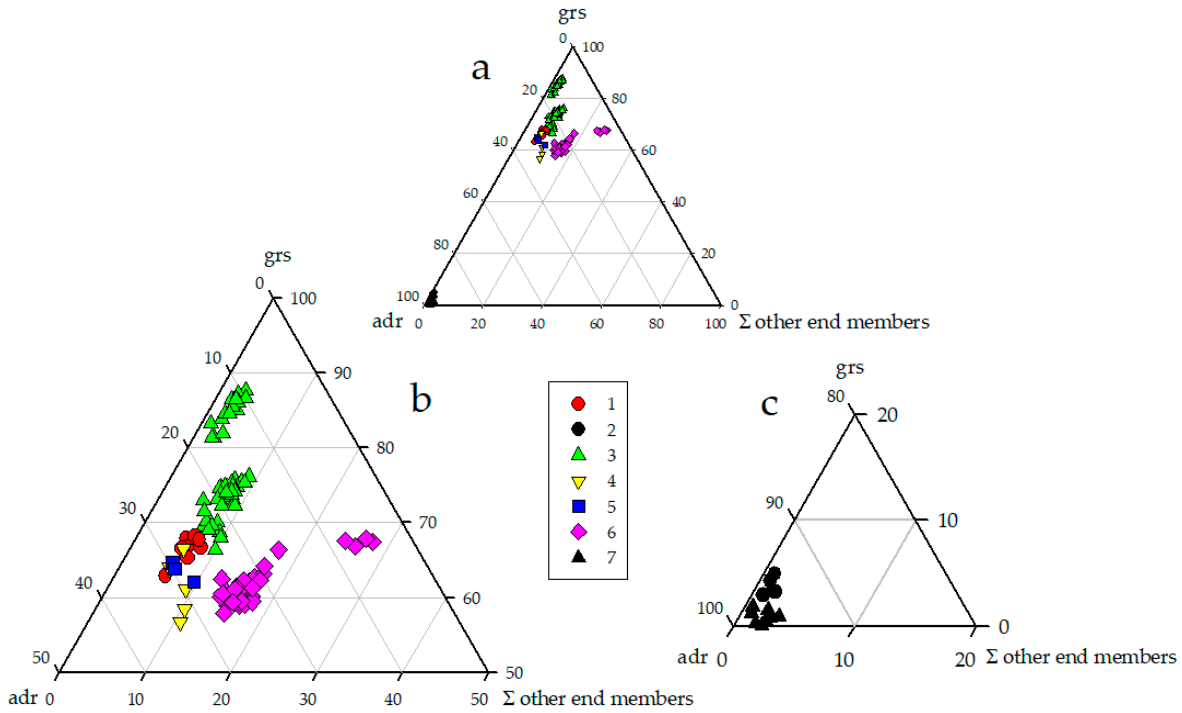

Figure 5. Compositional ternary diagram of grossular, andradite and the sum of remaining end-members of studied samples (**a**) and enlargements (**b**,**c**).

Table 6. LA–ICP–MS analyses of the Val d'Ala garnets (ppm).

Sample	2	7	1	3	6
	Average 6 pts	Average 13 pts	Average 5 pts	Average 5 pts	Average 9 pts
Sc	0.39	8.47	24.81	26.18	41.36
Ti	141.4	2296	8686	2255	8295
V	276.5	573.9	299.3	177.1	379.4
Cr	5.04	271.5	55.26	13.93	400.1
Co	0.01	0.06	1.58	3.78	2.14
Ni	0.14	1.16	0.70	0.51	0.88
Zn	0.06	0.45	1.96	2.30	4.60
Sr	0.14	0.07	0.36	0.19	1.54
Y	0.88	1.00	25.06	6.06	43.98
Zr	0.72	1.68	10.79	7.71	14.64
La	0.86	0.19	0.01	0.01	0.12
Ce	2.20	1.52	0.37	0.22	0.75
Pr	0.22	0.19	0.31	0.19	0.42
Nd	0.99	1.12	5.40	3.25	7.64
Sm	0.19	0.28	3.95	1.34	5.39
Eu	0.06	0.41	1.68	0.78	2.61
Gd	0.16	0.24	5.27	1.54	7.72
Tb	0.02	0.03	0.77	0.21	1.21
Dy	0.16	0.18	5.59	1.43	9.12
Ho	0.03	0.03	0.90	0.23	1.59
Er	0.09	0.07	2.77	0.62	4.90
Tm	0.01	0.01	0.32	0.06	0.58
Yb	0.10	0.09	2.68	0.46	4.72
Lu	0.01	0.01	0.31	0.05	0.55
∑REE	5.10	4.36	30.33	10.39	47.31

The deficiency of silica (stoichiometric Si values lower than 6 in Table 5) may indicate the possible occurrence of OH in the tetrahedral site supporting the presence of water as resulted from the Raman spectra (see below).

The results show two different compositions of garnets. The first group, including samples 2 and 7, is very close to the end member andradite; the second one (massive samples 1, 4, 5 and thin sections 3 and 6) belongs to a solid solution grossular–andradite (grandite), never reaching the grossular pure end member.

The aspect and the analyses of sample 2 (Adr_{96}) from Roch Neir II confirm the previous classification of garnet as topazolite, the variety of andradite greenish–yellow in color. Sample 7 from Mount Tovo with globular and rounded crystal shapes, reported in literature as grossular [3], is here determined to be 95–99% andradite. Sample 7 exhibits a hue of color ranging from green to orange–brown with higher content of the chromophore minor elements, such as Ti, Cr, and V. The higher content of these elements was determined in the brown zones of the crystals.

In the second group, including samples from deep red-brown to light orange in color and classified as hessonite variety, grossular content ranges from 41% to 88%, andradite content from 4% to 48% and almandine up to 20%. The higher grossular component was detected in samples from Testa Ciarva (sample 3) and Curbassera (sample 6) where garnets consist of large red brown crystals covered by smaller garnet crystals paler in color in respect to the samples from Roch Neir I (1), II (4,5). The TiO_2 content is up to 2.4 wt %, Cr_2O_3 ranges from nil to 0.1 wt %, and MnO from 0.3 wt % to 0.8 wt %. The variations, occurring in all samples, are not related to a regular or harmonic zoning from core to the rim. The lower content of chromophore elements (Ti, V, and Cr) of sample 3 (Testa Ciarva) may explain the color of faceted samples 11 and 12 coming from the same locality, lighter than those from Roch Neir II (9–11).

Examples of the compositional variations in Adr and Grs components are depicted in BSE images (samples 3 and 6): the garnet appears heterogenous with lighter parts enriched in andradite content (Figure 6a,b; Table 5, C1-6 and C3b-42 analyses) in respect to the darker ones (Figure 6a,b; Table 5, C1-1 and C3b-43 analyses).

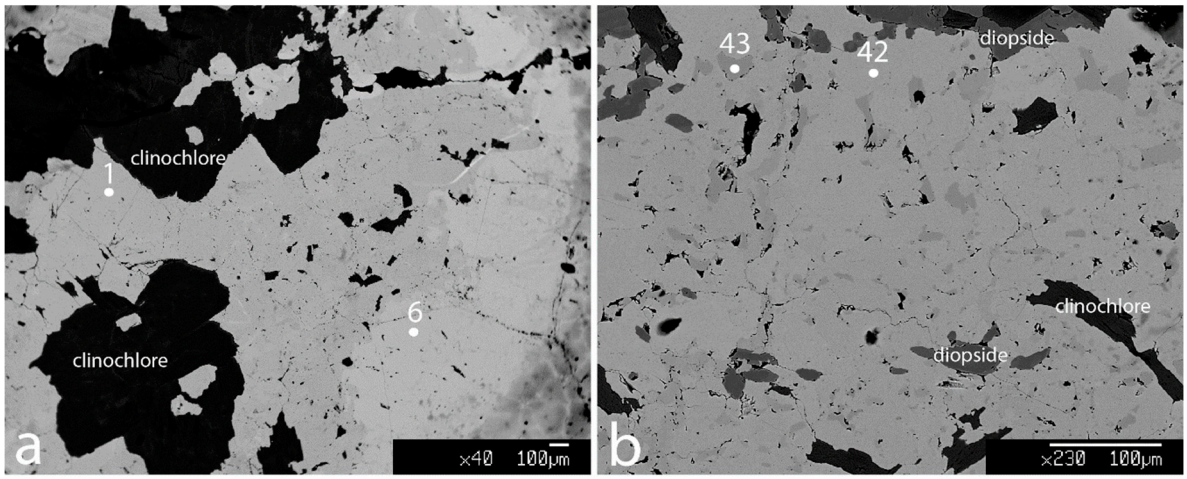

Figure 6. BSE images of garnets (dark and light gray) in sample 3 (**a**) and 6 (**b**). The numbers in the photos refer to microprobe point analyses in Table 5.

Chondrite-normalized REE patterns [28] of the examined samples are plotted, as mean values, in Figure 7a. The patterns of grandite garnets (1,3,6) display an increase of heavy rare earth elements (HREE) and well match that of grossular garnet. In contrast, andradite samples (2,7) show the enrichment in LREE with respect to HREE. As already discussed by [29] this behavior is controlled by crystal chemistry and indicate that in a calcic garnet the substitution of Fe^{3+} for Al at the [*Y*] site enlarges the eightfold [*X*] site and favors the incorporation of LREE. Moreover, the positive Eu anomaly,

more evident in sample 7 and in the andradite-rich areas of sample 3, implies the presence of Eu in the reduced form (Eu^{2+}) according with the reaction $Fe^{2+} + Eu^{3+} \rightarrow Fe^{3+} + Eu^{2+}$ [30] and its fractionation from the HREE.

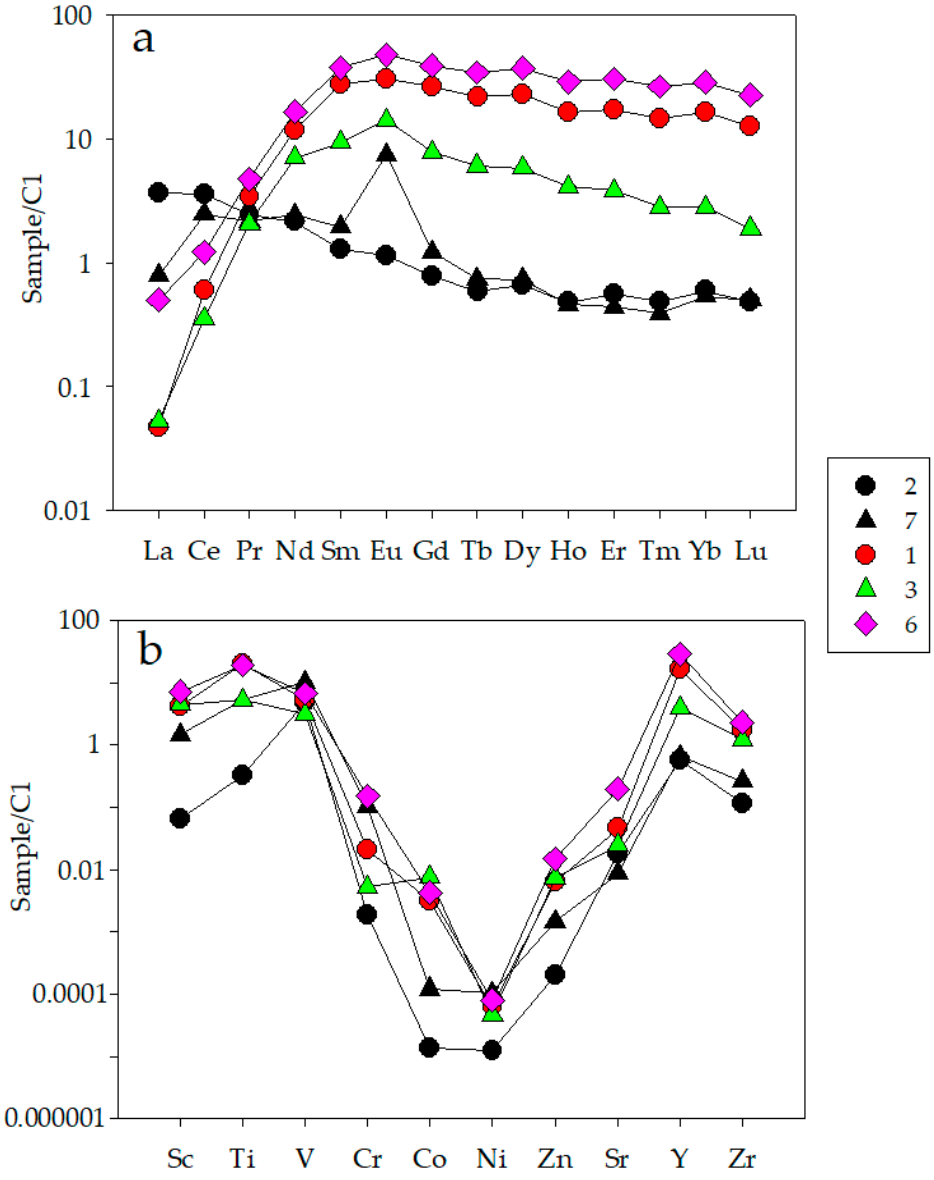

Figure 7. REE patterns (**a**) and multi-element diagram (**b**) for the analyzed samples.

In all samples, total REE content correlates positively with Y indicating, at least at local level, an equilibrium state [31]. Yttrium is plotted in the chondrite-normalized diagram together with the concentrations of Sr, Zr and of trace elements forming the "first transition series" (i.e., Sc, Ti, V, Cr, Co, Ni, and Zn), arranged according to the atomic number increasing (Figure 7b). The patterns are typically U-shaped and in all samples Cr, Co, Ni, Zn, and Y are below the C1 values whereas Sc, Ti, V, and Zr show a slight enrichment mainly in grandites. Other measured trace elements (Cs, Ba, Pb, Nb, Hf, Ta, Th, and U) resulted below the detection limits.

The calculated *a* unit-cell parameter from XRPD analyses, crystallite size and microstrain of the four analyzed samples are reported in Table 7. The *a*-value of samples 2 and 7 are in agreement with the end-member andradite, whereas in sample 1 the cell edge results between the grossular and andradite values reported in literature (andradite a = 12.0630(1) Å, value from [32]; grossular a = 11.8505(4) Å, value from [33]). XRPD pattern of sample 3 suggests the coexistence of two separate garnets, an almost

pure grossular (3-1) associated with an andradite (3-2). Note the occurrence of a second generation of little light yellow andradite-garnets formed on the older and bigger red grossular as suggested by [3].

Table 7. Crystallographic data.

Sample	*a* (Å)	Crystal Size (Å)	Microstrain
2 and 7	12.0633(3)	1610	0.004
1	11.9394(4)	1440	0.055
3-1	11.8826(3)	1510	0.031
3-2	12.0650(3)	-	-

The microstructural features of garnet 3-2 were not reported because of the low statistics of its diffraction peaks in the XRPD pattern that do not allow us to obtain reliable microstructural results.

The mean crystal size is larger for grossular (3-1) and andradite (2,7) than for the most intermediate grossular-andradite solid solution (1), reflecting the larger coherence of their diffracting domains. Conversely, the microstrain is smaller for grossular (3-1) and andradite (2,7) whereas the intermediate solid solution shows smaller crystallite sizes and larger strain values.

The presence of garnets with different morphology and crystal-chemistry is related to changing of chemical and physical conditions during the calcic metasomatism, which represents the main cause of the occurrence of rodingites in this area and/or during the subsequent Alpine deformation and metamorphism. The grandite garnets probably were formed in presence of low fO_2 fluids (low Adr/Alm ratio) during the serpentinization of the host rocks. On the contrary, the smaller and well-shaped andradites may be the product of an increase of fluid activity (fO_2~HM buffer) producing a progressive Al mobility and removal, accompanied by a significant increase in the iron oxidation (high Adr/Alm ratio) [18,34,35].

4.3. Raman and DRIFT Spectroscopy

We analyzed all the faceted garnets using the Raman spectroscopy from 100 cm^{-1} to 1100 cm^{-1} and from 3500 cm^{-1} to 3700 cm^{-1}; the range 100–1100 cm^{-1} is usually divided for garnets in two regions: the first below 400 cm^{-1} (internal vibrations) and the second above 400 cm^{-1} (external vibration region). All the spectra resulted very similar, so only that relative to sample 9 is shown in Figure 8.

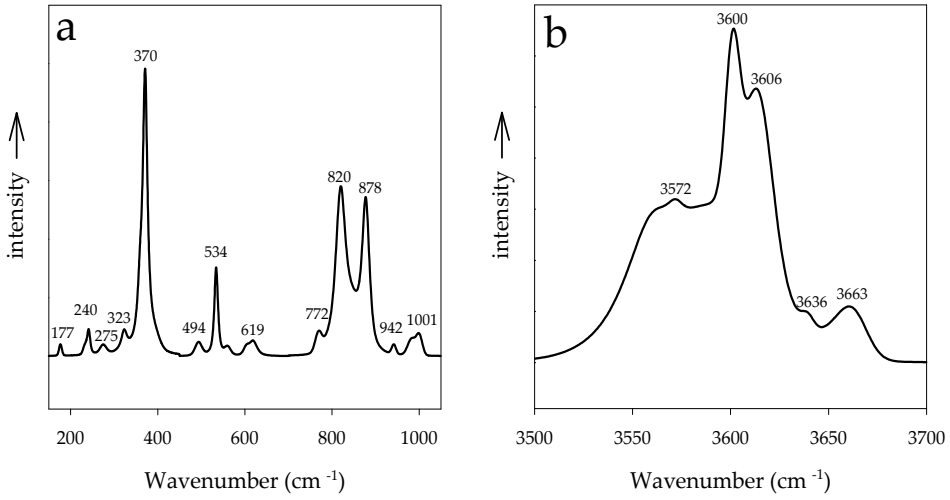

Figure 8. Raman spectra of sample 9 in the two considered ranges of frequency: (**a**) 100–1100 cm^{-1} and (**b**) 3500–3700 cm^{-1}.

In Figure 8a, the vibrations up to 320 cm^{-1} are attributed to SiO_4 tetrahedra and divalent cations translations (bands at 177 cm^{-1}, 241 cm^{-1}, 275 cm^{-1}) and between 320 cm^{-1} and 400 cm^{-1} to the

librations of the SiO_4 units (360, Si–O–O bending motions within the SiO_4 groups). Between 400 cm^{-1} and 650 cm^{-1} one observes the O–Si–O bending modes (bands at 494 cm^{-1}, 534 cm^{-1}, 561 cm^{-1}, 619 cm^{-1}) whereas at frequencies higher than 800 cm^{-1} the Si–O stretching modes (bands at 820 cm^{-1}, 878 cm^{-1}, 942 cm^{-1}, 1001 cm^{-1}) [36–38]. Table 8 presents the main peaks of the grossular and andradite end-members and those present in our samples (indicated as "This work") resulted consistent, by comparison, with a solid solution of grossular and andradite.

Table 8. Raman frequency (cm^{-1}) of selected peaks of andradite and grossular end members and our results.

	Peak #1	This Work	Peak #2–#3	This Work	Peak #4	This Work	Peak #5	This Work	Peak #6	This Work
Andradite	236	240	352–370	370	516	534	816	820	874	878
Grossular	247		373–376		550		827		880	

Moreover, the analysis of the Raman spectrum in the range from 3500 cm^{-1} to 3700 cm^{-1} allowed us to determine the presence of OH, that, in grossular garnets and especially in rodingites, may be present (expressed as weight % in H_2O) in a range from 12.8 wt % to less than 0.005 wt % but typically less than 0.3 wt % [39]. In Figure 8b, we can observe the internal OH-stretching modes that derive from the O_4H_4 groups. The OH-stretching region consists of two OH bands around 3663 cm^{-1} and 3600 cm^{-1}. The 3663 cm^{-1} band is connected to vibrations of O_4H_4 groups that are surrounded by other O_4H_4 groups and the 3600 cm^{-1} band to O_4H_4 clusters adjacent to their SiO_4 neighbors [39]. The more complex bands at 3606 cm^{-1} and 3636 cm^{-1} are OH-stretching modes [40]. The band located at 3572 cm^{-1} may represent hydrogrossular substitution [41,42].

The infrared spectra between 1100 cm^{-1} and 450 cm^{-1} of samples 2 and 7 and of samples 3 and 4 are very similar to each other. Spectra of samples 2 and 3 are shown in Figure 9. The sample 2 exhibits peaks at 888 cm^{-1}, 830 cm^{-1} and 815 cm^{-1}, 589 cm^{-1}, 511 cm^{-1}, and 478 cm^{-1}, which are related to the vibrational mode of the SiO_4 tetrahedra [43–45]. The position of these peaks are in agreement with measurements relative to andradite (94%) of [43] and are consistent with our chemical results on this sample (andradite 96%). Instead, the spectra of sample 3, resulted 61% grossular, shows a shift of these SiO_4 vibrational modes towards higher frequency, i.e., 908 cm^{-1}, 853 cm^{-1} and 837 cm^{-1}, 615 cm^{-1}, 538 cm^{-1}, and 468 cm^{-1}, consistent with data reported in [45] for grossular and in [43] for 74% grossular. The change of the energies of these mid-IR bands is due to difference in the chemical composition, as well known for garnets.

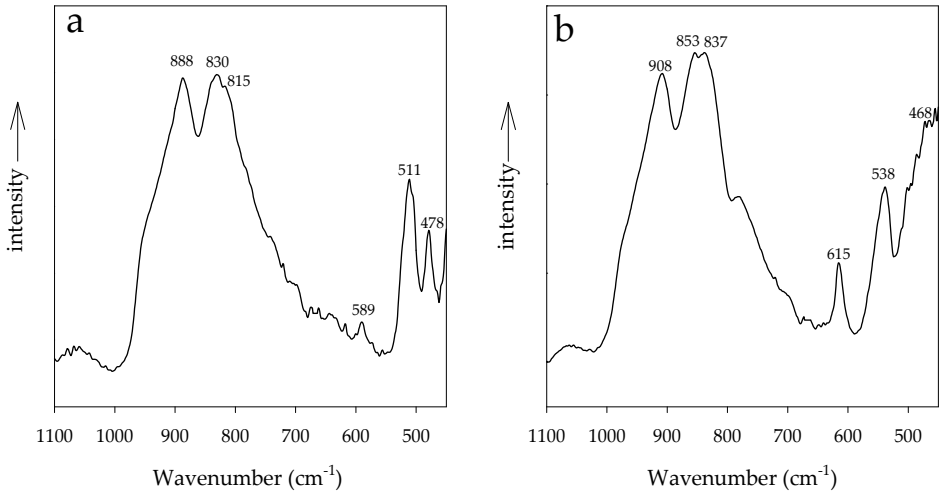

Figure 9. Infrared absorption spectra of samples 2 (**a**) and 3 (**b**).

5. Conclusions

Ca-rich garnets are the only documented garnets occurring in the rodingites of Val d'Ala. The orange–red garnets from Testa Ciarva and the light yellow colored andradite (topazolite variety) from Roch Neir I are prized among gemstone collectors. The variation in color make them very attractive and valuable for gemological purposes. However, the translucent diaphaneity and the presence of defects and fractures (well evidenced by the μCT) which characterize their singular charm, motivated the scarce consideration on the market for these garnets.

The complete characterization we carried out leads to the following conclusions:

Chemical composition ranges from grossular-andradite solid solution to pure andradite. These compositional variations resulted irregular and indicate, together with the different size of the crystals, a growth in partial chemical equilibrium conditions, as expected in polyphasic metamorphic rocks. The crystallization of both Grs rich and pure Adr garnet suggests a change from internally buffered metamorphic conditions to infiltration processes of oxidation fluids, probably released by the hosting serpentinite, both during oceanization and subduction processes, in agreement with the metamorphic evolution inferred from the literature (Figure 2d). Indeed, Val d'Ala metaophiolites recorded low-pressure re-equilibration during Jurassic-Cretaceous oceanization, followed by eclogite- and greenschist-facies imprints during Alpine subduction and successive exhumation.

Crystallographic data highlight the coexistence of almost pure andradite and grandite very close to grossular end-member enlarging the variation range resulted from microprobe analyses.

The DRIFT spectra result adequate to the chemical compositions. Raman spectra of faceted samples resulted in andradite-grossular solid solution and evidenced the presence of OH but at a very low level.

Compositional variation, microstructure, and growth zoning of garnet may be used as a key to understanding the timing and duration of the metamorphic events or the partial chemical equilibrium during the crystallization. In a complex geological context such as that of Val d'Ala, the present data, suggest a growth of garnets during one or more metasomatic/metamorphic events, involving increasing of Ca and variation of Al and Fe mobility due to different influx of hydrothermal fluids and/or different chemical and physical interaction with the host rocks.

A forthcoming planned structural and metamorphic analysis supporting a strategic sampling, focused on defining the relative chronology of overlapping tectono-metamorphic imprints, will drive towards a comprehensive interpretation of the geological and petrological processes occurred in Val d'Ala metaophiolites.

Author Contributions: V.D. performed EMPA analyses; N.M. the XRD analysis; L.M. the Synchrotron X-ray computed micro-tomography; M.I.S. is responsible for thin sections analysis and geological outline; A.L. collected LA–ICP–MS data; F.C. characterized the gemological materials and performed the Raman analyses; I.A. performed the DRIFT analyses; V.D., R.B., M.I.S., N.M., and F.C. analyzed the data and wrote the paper. All authors contributed to the final version and gave their approval for submission.

Funding: This research received no external funding.

Conflicts of Interest: The authors declare no conflict of interest.

References

1. Repossi, E. La Val d'Ala e i suoi minerali. *Riv. Sci. Nat.* **1919**, *10*, 89–132.
2. Grill, E. Quarzo, granato, clorite di Val d'Ala. *Atti Soc. Ital. Sci. Nat.* **1922**, *61*, 215–240.
3. Grill, E.; Repossi, E. Itinerari Mineralogici. *Riv. Sci. Nat.* **1942**, *33*, 96–111.
4. Maletto, G.; Piccoli, G.C. *Minerali in Val d'Ala*; Ass. Amici del Museo F. Eusebio: Cuneo, Italy, 2014; p. 224, ISBN-10 8890380985, ISBN-13 9788890380983.
5. Coleman, R.G. *Low-Temperature Reaction Zones and Alpine Ultramafic Rocks of California, Oregon, and Washington*; U.S. Geological Survey Bulletin: Washington, DC, USA, 1967; Volume 1247, pp. 1–49.
6. Dal Piaz, G.V. Le «granatiti» (rodingiti l.s.) nelle serpentine delle Alpi occidentali italiane. *Mem. Soc. Geol. Ital.* **1967**, *6*, 267–313.

7. Austrheim, H.; Prestvik, T. Rodingitization and hydration of the oceanic lithosphere as developed in the Leka ophiolite, north–central Norway. *Lithos* **2008**, *104*, 177–198. [CrossRef]
8. Frost, B.R.; Beard, J.S.; McCaig, A.; Condliffe, E. The Formation of Micro-Rodingites from IODP Hole U1309D: Key to Understanding the Process of Serpentinization. *J. Petrol.* **2008**, *49*, 1579–1588. [CrossRef]
9. Piccardo, G.B.; Messiga, B.; Cimmino, F. Antigoritic serpentinites and rodingites of the Voltri Massif: Some petrological evidences for their evolutive history. *Ofioliti* **1980**, *5*, 111–114.
10. Li, X.-P.; Rahn, M.; Bucher, K. Metamorphic Processes in Rodingites of the Zermatt-Saas Ophiolites. *Int. Geol. Rev.* **2004**, *46*, 28–51. [CrossRef]
11. Li, X.-P.; Rahn, M.; Bucher, K. Eclogite facies metarodingites—Phase relations in the system SiO_2-Al_2O_3-Fe_2O_3-FeO-MgO-CaO-CO_2-H_2O: An example from the Zermatt-Saas ophiolite. *J. Metamorph. Geol.* **2008**, *26*, 347–364. [CrossRef]
12. Ferrando, S.; Frezzotti, M.L.; Orione, P.; Conte, R.C.; Compagnoni, R. Late-Alpine rodingitization in the Bellecombe meta-ophiolites (Aosta Valley, Italian Western Alps): Evidence from mineral assemblages and serpentinization-derived H2-bearing brine. *Int. Geol. Rev.* **2010**, *52*, 1220–1243. [CrossRef]
13. Zanoni, D.; Rebay, G.; Bernardoni, J.; Spalla, M.I. Using multiscale structural analysis to infer high-/ultrahigh-pressure assemblages in subducted rodingites of the Zermatt-Saas Zone at Valtournanche, Italy. *J. Virtual Explor.* **2012**, *41*, 2–30. [CrossRef]
14. Zanoni, D.; Rebay, G.; Spalla, M.I. Ocean floor and subduction record in the Zermatt-Saas rodingites, Valtournanche, Western Alps. *J. Metamorph. Geol.* **2016**, *34*, 941–961. [CrossRef]
15. Leardi, L.; Rossetti, P.; Compagnoni, R. Geochemical study of a metamorphic ophiolite sequence from the Val d'Ala di Lanzo (internal Piedmontese Zone, Graian Alps, Italy). *Mem. Soc. Geol. Ital.* **1984**, *29*, 93–105.
16. Leardi, L.; Rossetti, P. Caratteri geologici e petrografici delle metaofioliti della Val d'Ala (Valli di Lanzo, Alpi Graie). *Boll. Dell'assoc. Min. Subalp.* **1985**, *XXII*, 422–441.
17. Sandrone, R.; Leardi, L.; Rossetti, P.; Compagnoni, R. P-T conditions for the eclogitic re-equilibration of the metaophiolite from Val d'Ala (internal Piemontese zone, Western Alps). *J. Metamorph. Geol.* **1986**, *4*, 161–178. [CrossRef]
18. Laborda-López, C.; Sánchez-Vizcaíno, V.L.; Marchesi, C.; Gómez-Pugnaire, M.T.; Garrido, C.J.; Jabaloy-Sánchez, A.; Padrón-Navarta, J.A.; Hidas, K. High-P metamorphism of rodingites during serpentinite dehydration (Cerro del Almirez, Southern Spain): Implications for the redox state in subduction zones. *J. Metamorph. Geol.* **2018**, *36*, 1141–1173. [CrossRef]
19. Dal Piaz, G.V. Filoni rodingitici e zone di reazione a bassa temperatura al contatto tettonico tra serpentine e rocce incassanti nelle Alpi occidentali italiane. *Rend. Soc. Ital. Mineral. Petrol.* **1969**, *25*, 262–315.
20. Mattirolo, E.; Novarese, V.; Franchi, S.; Stella, A. *Carta Geologica D'italia Alla Scala 1:100.000*; Foglio 55; Servizio Geologico d'Italia: Susa, Italy, 1910.
21. Spear, F.S. *Metamorphic Phase Equilibria and Pressure-Temperature-Time Paths*; Mineralogical Society of America Special Publication: Washington, DC, USA, 1993; p. 799.
22. Feldkamp, L.A.; Davis, L.C.; Kress, J.W. Practical cone-beam algorithm. *J. Opt. Soc. Am. A* **1984**, *1*, 612–619. [CrossRef]
23. Kitchen, M.J.; Pavlov, K.M.; Siu, K.K.W.; Menk, R.H.; Tromba, G.; Lewis, R.A.; Pavlov, K. Analyser-based phase contrast image reconstruction using geometrical optics. *Phys. Med. Biol.* **2007**, *52*, 4171–4187. [CrossRef]
24. Rietveld, H.M. A profile refinement method for nuclear and magnetic structures. *J. Appl. Crystallogr.* **1969**, *2*, 65–71. [CrossRef]
25. Toby, B.H.; Von Dreele, R.B. GSAS-II: The genesis of a modern open-source all purpose crystallography software package. *J. Appl. Crystallogr.* **2013**, *46*, 544–549. [CrossRef]
26. Johnson, M.L.; Boehm, E.; Krupp, H.; Zang, J.W.; Kammerling, R.C. Gem-Quality Grossular-Andradite: A New Garnet from Mali. *Gems Gemol.* **1995**, *31*, 152–166. [CrossRef]
27. Droop, G.T.R. A general equation for estimating Fe3+concentrations in ferromagnesian silicates and oxides from microprobe analyses, using stoichiometric criteria. *Mineral. Mag.* **1987**, *51*, 431–435. [CrossRef]
28. Anders, E.; Grevesse, N. Abundances of the elements: Meteoritic and solar. *Geochim. Cosmochim. Acta* **1989**, *53*, 197–214. [CrossRef]
29. Bocchio, R.; Adamo, I.; Diella, V. The profile of trace elements, including the REE, in gem-quality green andradite from classic localities. *Can. Miner.* **2010**, *48*, 1205–1216. [CrossRef]

30. Sverjensky, D.A. Europium redox equilibria in aqueous solution. *Earth Planet. Sci. Lett.* **1984**, *67*, 70–78. [CrossRef]
31. Park, C.; Song, Y.; Kang, I.-M.; Shim, J.; Chung, D.; Park, C.-S. Metasomatic changes during periodic fluid flux recorded in grandite garnet from the Weondong W-skarn deposit, South Korea. *Chem. Geol.* **2017**, *451*, 135–153. [CrossRef]
32. Armbruster, T.; Geiger, C.A. Andradite crystal chemistry, dynamic X-site disorder and structural strain in silicate garnets. *Eur. J. Miner.* **1993**, *5*, 59–72. [CrossRef]
33. Rodehorst, U.; Geiger, C.A.; Armbruster, T. The crystal structures of grossular and spessartine between 100 and 600 K and the crystal chemistry of grossular-spessartine solid solutions. *Am. Miner.* **2002**, *87*, 542–549. [CrossRef]
34. Basso, R.; Cimmino, F.; Messiga, B. Crystal chemical and petrological study of hydrogarnets from a Fe-gabbro metarodingites (Gruppo di Voltri, Western Liguria, Italy). *Neues Jahrb. Mineral. Abh.* **1984**, *150*, 247–258.
35. Dubińska, E.; Bylina, P.; Kozłowski, A. Garnets from Lower Silesia rodingites: Constraints from their chemistry. *Mineral. Soc. Pol. Spec. Pap.* **2004**, *24*, 135–139.
36. Kolesov, B.A.; Geiger, C.A. Raman scattering in silicate garnets: An investigation of their resonance intensities. *J. Raman Spectrosc.* **1997**, *28*, 659–662. [CrossRef]
37. Kolesov, B.A.; Geiger, C.A. Raman spectra of silicate garnets. *Phys. Chem. Miner.* **1998**, *25*, 142–151. [CrossRef]
38. Bersani, D.; Ando, S.; Vignola, P.E.; Moltifiori, G.; Marino, I.-G.; Lottici, P.P.; Diella, V. Micro-Raman spectroscopy as a routine tool for garnet analysis. *Spectrochim. Acta Part A Mol. Biomol. Spectrosc.* **2009**, *73*, 484–491. [CrossRef]
39. Rossmann, G.R.; Aines, R.D. The hydrous component in garnets: Grossular–hydrogrossular. *Am. Mineral.* **1991**, *76*, 1153–1164.
40. Thomas, S.-M.; Davidson, P.; Reichart, P.; Koch-Müller, M.; Dollinger, G. Application of Raman spectroscopy to quantify trace water concentrations in glasses and garnets. *Am. Mineral.* **2008**, *93*, 1550–1557. [CrossRef]
41. Lager, G.A.; Armbruster, T.; Rotella, F.J.; Rossmann, G.R. OH substitution in garnets: X-ray and neutron diffraction, infrared and geometric modeling studies. *Am. Mineral.* **1989**, *74*, 840–851.
42. Andrut, M.; Wildner, M.; Beran, A. The crystal chemistry of birefringent natural uvarovites. Part IV. OH defect incorporation mechanisms in non-cubic garnets derived from polarized IR spectroscopy. *Eur. J. Miner.* **2002**, *14*, 1019–1026. [CrossRef]
43. Moore, R.K.; White, W.B.; Long, T.V. Vibrational spectra of the common silicates: I. The garnets. *Am. Mineral.* **1971**, *56*, 54–71.
44. Hofmeister, A.; Chopelas, A. Vibrational spectroscopy of end-member silicate garnets. *Phys. Chem. Miner.* **1991**, *17*, 503–526. [CrossRef]
45. Bosenick, A.; Geiger, C.A.; Schaller, T.; Sebald, A. A 29 Si MAS NMR and IR spectroscopic investigation of synthetic pyrope-grossular garnet solid solutions. *Am. Mineral.* **1995**, *80*, 691–704. [CrossRef]